



Laser light propagation in a turbid medium: solution including multiple scattering effects

Knut Stamnes^{1,a}, Wei Li^{1,b}, Snorre Stamnes^{2,c}, Yong Hu^{2,d}, Yingzhen Zhou^{1,e}, Nan Chen^{1,f}, Yongzhen Fan^{3,g}, Børge Hamre^{4,h}, Xiaomei Lu^{2,i}, Yuping Huang^{1,j}, Carl Weimer^{5,k}, Jennifer Lee^{5,l}, Xubin Zeng^{6,m}, and Jakob Stamnes^{4,n}

¹ Department of Physics, Stevens Institute of Technology, 1 Castle Point on Hudson, Hoboken, NJ 07030, USA

² Langley Research Center, NASA, Hampton, VA, USA

³ Earth System Science Interdisciplinary Center (ESSIC), University of Maryland, College Park, MD, USA

⁴ Department of Physics, University of Bergen, Bergen, Hordaland, Norway

⁵ Ball Aerospace, Boulder, CO, USA

⁶ Department of Hydrology and Atmospheric Science, The University of Arizona, Tucson, AZ, USA

Received 29 December 2022 / Accepted 30 May 2023 / Published online 19 June 2023

© The Author(s) 2023

Abstract.

We have shown that solutions to the radiative transfer equation for a homogeneous slab yield a zenith radiance reflectance that for collimated beam incidence in the nadir direction can be expressed in terms of the lidar ratio, defined as the extinction coefficient divided by the 180° backscattering coefficient. The recently developed **QIbIC** method, which allows one to quantify layer-by-layer contributions to radiances emerging from a slab illuminated with a collimated beam of radiation, was used to show explicitly that in the single-scattering approximation the attenuated backscatter coefficient estimated by the new **QIbIC** method gives the same result as the lidar equation. Originally developed for the continuous wave (CW) lidar problem, we have extended the new **QIbIC** method to apply to the pulsed lidar problem. A specific example is provided to illustrate the challenge encountered for ocean property retrievals from space observations due to the fact that a very significant fraction of the signal is due to aerosol scattering/absorption; typically only about 10% (or less) comes from the ocean.

1 Introduction

The United States National Academy of Sciences, Engineering, and Medicine 2017 Decadal Survey, ‘Thriving

Wei Li, Snorre Stamnes, Yong Hu, Yingzhen Zhou, Nan Chen, Yongzhen Fan, Børge Hamre, Xiaomei Lu, Yuping Huang, Carl Weimer, Jennifer Lee, Xubin Zeng and Jakob Stamnes have contributed equally to this work.

^a e-mail: kstamnes@stevens.edu (corresponding author)

^b e-mail: wli4@stevens.edu

^c e-mail: snorre.a.stamnes@nasa.gov

^d e-mail: yongxiang.hu-1@nasa.gov

^e e-mail: yzhou64@stevens.edu

^f e-mail: Nan.Chen@stevens.edu

^g e-mail: yfan1236@umd.edu

^h e-mail: Borge.Hamre@uib.no

ⁱ e-mail: xiaomei.lu@nasa.gov

^j e-mail: yhuang5@stevens.edu

^k e-mail: Carl.Weimer@ballaerospace.com

^l e-mail: Jennifer.Lee@ballaerospace.com

^m e-mail: xubin@arizona.edu

ⁿ e-mail: Jakob.Stamnes@uib.no

on Our Changing Planet: A Decadal Strategy for Earth Observations from Space’ calls for a lidar and polarimeter to accurately characterize vertically resolved absorbing and scattering properties of aerosols. The lidar is expected to be at least as capable as the Cloud Aerosol Lidar with Orthogonal Polarization (CALIOP) instrument, which has been shown to enable retrievals of aerosol, cloud, and ocean products from space. In addition, the next generation of airborne lidars includes high spectral resolution lidars (HSRL) with the capability for aerosol measurements at 1064, 532, and 355 nm [1] and ocean measurements at 532 and 355 nm [2]. These advanced, powerful lidar systems require new algorithms in order to accurately and efficiently account for multiple scattering in cirrus and water clouds as well as in open ocean waters and coastal waters with high levels of particulate scattering. For spaceborne lidar systems, multiple scattering leads to a significant contribution to lidar returns [3].

Although Monte Carlo (MC) algorithms exist for elastic backscatter lidar like CALIOP, it is highly desirable to have access to an efficient yet accurate forward radiative transfer model that will be significantly faster

than existing MC algorithms in simulating lidar signals due to multiple scattering in cirrus and water clouds as well as coastal water.

Reliable interpretation of lidar/radar returns from the atmosphere (or lidar returns from the ocean) relies on accurate solutions of a forward/inverse problem. To solve the inverse problem, it is very useful to have access to a fast yet accurate forward model. For continuous-wave lidar/radar beam illumination, one needs to solve the steady-state (time-independent) radiative transfer equation (RTE) for beam propagation including multiple scattering throughout the medium (atmosphere or ocean). However, most active remote sensing techniques rely on illumination using lidar/radar pulses, implying that one must solve the time-dependent RTE. For a space-based lidar, such as the CALIOP instrument, which has operated in space since 2006 on the Cloud Aerosol Lidar and Infrared Pathfinder Satellite Observation (CALIPSO) platform, one needs to solve the time-dependent RTE for the coupled atmosphere-ocean system in order to infer water parameters from space [4–6].

Many retrieval algorithms ignore or treat multiple scattering in an approximate manner, which may yield unreliable results. For example, it has been shown that if lidar multiple-scattering effects were omitted in combined radar-lidar retrievals of ice clouds from space, the retrieved optical depth might be underestimated by as much as 40% [7]. Therefore, to fully understand and exploit the information contained in received lidar/radar returns, one should have access to accurate methods to assess the error incurred by ignoring or not including multiple scattering effects in an accurate manner. Exploring to what extent multiple scattering can be used as an additional source of retrievable information about medium properties is also an important issue that deserves serious attention [8].

Radiative transfer involving lidar/radar (finite) beam illumination is a three-dimensional (3-D) problem. The solution of the 3-D RTE for a narrow finite laser beam (i.e., the so-called searchlight problem) is quite challenging and computationally demanding. Therefore, it has become customary to use a one-dimensional (1-D) approach instead, and most treatments of the lidar/radar problem rely on solving a 1-D RTE for both atmospheric [9,10] and oceanic [11] applications.

2 Summary of single-scattering results

Solving the radiative transfer equation (RTE) pertinent for a collimated beam of light that is incident upon a slab of optical thickness τ_b , we find the radiance reflectance in the single-scattering approximation (SSA) to be given by [see Eqs. (A21) and (A18) in Appendix A]:

$$R_{I,SSA} = \frac{1}{2S}(1 - e^{-2\tau_b}) \tag{1}$$

where the lidar ratio S (i.e., the extinction coefficient divided by the 180° backscattering coefficient) depends on the scattering phase function, $p(\cos \Theta)$: $S = S_{\text{iso}} = 4\pi$ for isotropic scattering, $p_{\text{iso}}(\cos \Theta) = 1.0$; $S = S_{\text{Ray}} = \frac{8\pi}{3}$ for Rayleigh scattering, $p_{\text{Ray}}(\cos \Theta) = \frac{3}{4}(1 + \cos^2 \Theta)$; $S = S_{\text{HG}} = \frac{4\pi(1+g)^2}{(1-g)}$ for Henyey–Greenstein (HG) scattering, $p_{\text{HG}}(\cos \Theta) = (1-g^2)/(1+g^2 - 2g \cos \Theta)^{3/2}$, where Θ is the scattering angle (Eq. (A13)) and g is the asymmetry factor of the scattering phase function.

The advantage of solving the RTE in a slab geometry, which leads to the SSA result in Eq. (1), is that it yields valid results also when multiple-scattering effects prevail. However, a slab geometry, on which Eq. (1) is based, does not apply to a laser beam of finite lateral extent. Nevertheless, Eq. (1) is expected to be a reasonable approximation when the scattering mean free path is less than the lateral extent of the laser beam.

The Quantification of layer-by-layer Contribution (Qlbic) method [12] can be used to estimate the backscatter attenuation coefficient for the lidar problem as outlined in Sect. 3.1. In Sect. 3.3, we show explicitly that a single-scattering estimate based on the Qlbic method [see Eq. (10)] gives the same result as the lidar equation [see Eq. (11)] for the attenuated backscatter coefficient [see Eq. (12)].

3 Results

3.1 The Qlbic method

Let’s consider a medium consisting of two adjacent, horizontal, multilayered coupled slabs illuminated from the top of the upper slab by a collimated beam of irradiance F_0 in direction θ_0 with respect to the normal to the two adjacent slabs. As discussed elsewhere [12], the radiative transfer equation (RTE) for such a problem can be solved by integrating the source function $S_i^\pm(t, \mu, \phi)$ ($i = n$, or p (layer indices) in Eqs. (2) and (3)) layer by layer to yield the following expressions for the Stokes vector $I^\pm(\tau, \mu, \phi)$ of the diffuse total and polarized radiance (the $+$ sign denotes the upward hemisphere while the $-$ sign denotes the downward hemisphere):

$$I^+(\tau, \mu, \phi) = \int_\tau^{\tau_p} \frac{dt}{\mu} S_p^+(t, \mu, \phi) e^{-(t-\tau)/\mu} + \sum_{n=p+1}^L \int_{\tau_{n-1}}^{\tau_n} \frac{dt}{\mu} S_n^+(t, \mu, \phi) e^{-(t-\tau)/\mu} \tag{2}$$

$$I^-(\tau, \mu, \phi) = \sum_{n=1}^{p-1} \int_{\tau_{n-1}}^{\tau_n} \frac{dt}{\mu} S_n^-(t, \mu, \phi) e^{-(\tau-t)/\mu} + \int_{\tau_{p-1}}^{\tau} \frac{dt}{\mu} S_p^-(t, \mu, \phi) e^{-(\tau-t)/\mu}. \tag{3}$$

Here τ is the optical depth, $\mu = |(\cos \theta)|$ (θ is the polar angle), and ϕ is the azimuthal angle. Since the source function $\mathbf{S}_i^\pm(t, \mu, \phi)$ in layer denoted by subscript i ($= n$, or p) can be evaluated analytically by the discrete ordinate method, the integrals in Eqs. (2) and (3) have analytic solutions.

Note that Eqs. (2) and (3) allow us to quantify the contributions from any specific layer in a single slab or any layer in either of two adjacent slabs with different refractive indices. For example, if we are interested in the contribution from layer M in either of the two adjacent slabs to the zenith radiance emerging from the top of the upper slab, we may proceed as follows:

- Compute $\mathbf{I}^+(\tau = 0, \mu = 1)$ by integrating all layers from the top of the upper slab including layer M ;
- Repeat the computation by integrating all layers from the top of the upper slab including layer $M - 1$;
- Subtract the latter result from the former to obtain the contribution from layer M .

Alternatively, we may obtain the same result by simply setting the source function to zero in all layers except in layer M , which is the layer of interest.

3.1.1 Emergent radiances

Evaluating Eq. (2) at $\tau = 0$ and $\mu = 1$ (ϕ irrelevant), we obtain the upward total and polarized radiance in the zenith direction $\mathbf{I}^+(0, 1)$ (relevant for spaceborne lidar deployments), while evaluating Eq. (3) at $\tau = \tau_L$ and $\mu = 1$ (ϕ irrelevant), we obtain the downward total and polarized radiance in the nadir direction $\mathbf{I}^-(\tau_L, 1)$ (relevant for ground-based lidar deployments):

$$\begin{aligned} \mathbf{I}^+(0, 1) &= \mathbf{I}^+(\tau = \tau_0 = 0, \mu = 1) \\ &= \sum_{n=1}^L \int_{\tau_{n-1}}^{\tau_n} dt \mathbf{S}_n^+(t, \mu = 1) e^{-t} \end{aligned} \tag{4}$$

$$\begin{aligned} \mathbf{I}^-(\tau_L, 1) &= \mathbf{I}^-(\tau = \tau_L, \mu = 1) \\ &= \sum_{n=1}^L \int_{\tau_{n-1}}^{\tau_n} dt \mathbf{S}_n^-(t, \mu = 1) e^{-(\tau_L-t)}. \end{aligned} \tag{5}$$

3.2 A simple two-layer model

As a simple example, consider a single slab (as opposed to two adjacent, coupled slabs) consisting of two layers ($L = 2$): a “target” (layer 2) overlain by layer 1. The slab is assumed to be illuminated by a collimated beam at an angle θ_0 . For this two-layer system, the reflected signal would be given by:

$$\mathbf{I}^+(0, 1) = \int_{\tau_0}^{\tau_1} dt \mathbf{S}_1^+(t, 1) e^{-t} + \int_{\tau_1}^{\tau_2} dt \mathbf{S}_2^+(t, 1) e^{-t}. \tag{6}$$

3.2.1 Single-scattering approximation (SSA)

Assuming that the single-scattering approximation is applicable for each of layers 1 and 2, we have (see Eq. (A3))

$$S_i^+(t, \mu) \equiv S_i^+(t, -\mu_0, \mu) \approx X_i^+(-\mu_0, \mu) e^{-t/\mu_0} \quad i = 1, 2 \tag{7}$$

where we have ignored polarization ($\mathbf{S}_i^+ \rightarrow S_i^+$) and $\mu_0 = \cos \theta_0$. If we consider both layers to be homogeneous and to scatter in accordance with the Henyey–Greenstein scattering phase function, $p_{\text{HG}}(-\mu_0, \mu, g_i)$ with asymmetry factor g_i , then

$$\begin{aligned} X_i^+(-\mu_0, \mu) &= \frac{\varpi_i F_0}{4\pi} p_{\text{HG}}(-\mu_0, \mu, g_i) \\ &\rightarrow \frac{\varpi_i F_0}{4\pi} p_{\text{HG}}(-1, 1, g_i) \quad i = 1, 2 \end{aligned}$$

for $\mu = \mu_0 = 1$. Hence, for incident beam irradiance $F_0 = 1.0$ (normal to the beam direction), the radiance reflectance becomes ($S_i^+(t, 1) = X_i^+(-1, 1) e^{-t}$)

$$\begin{aligned} R_{I, \text{SSA}} &= I^+(0, 1) = X_1^+(-1, 1) \int_{\tau_0}^{\tau_1} dt e^{-2t} \\ &\quad + X_2^+(-1, 1) \int_{\tau_1}^{\tau_2} dt e^{-2t} \end{aligned}$$

or (setting $\tau_0 = 0$ at the top of the upper slab)

$$\begin{aligned} R_{I, \text{SSA}} &= I^+(0, 1) = \frac{\varpi_1 (1 - g_1)}{8\pi (1 + g_1)^2} [1 - e^{-2\tau_1}] \\ &\quad + \frac{\varpi_2 (1 - g_2)}{8\pi (1 + g_2)^2} [e^{-2\tau_1} - e^{-2\tau_2}] \end{aligned}$$

or

$$\begin{aligned} R_{I, \text{SSA}} &= I^+(0, 1) = \frac{\varpi_1}{2\mathcal{S}_1} [1 - e^{-2\tau_1}] \\ &\quad + \frac{\varpi_2}{2\mathcal{S}_2} [e^{-2\tau_1} - e^{-2\tau_2}] \end{aligned} \tag{8}$$

where $\mathcal{S}_i = \mathcal{S}_{i, \text{HG}} = \frac{4\pi(1+g_i)^2}{(1-g_i)}$ ($i = 1, 2$) is the lidar ratio, defined as the extinction coefficient divided by the 180° backscattering coefficient, and g_i is the asymmetry factor of the scattering phase function, the only input parameter required for the HG phase function. Clearly, if the two layers have identical optical properties, i.e., if $\frac{\varpi_2}{2\mathcal{S}_2} = \frac{\varpi_1}{2\mathcal{S}_1} = \frac{\varpi}{2\mathcal{S}} = \frac{\varpi}{8\pi} \frac{(1-g)}{(1+g)^2}$, then $R_{I, \text{SSA}} = \frac{\varpi}{8\pi} \frac{(1-g)}{(1+g)^2} [1 - e^{-2\tau_b}] = \frac{\varpi}{2\mathcal{S}_{\text{HG}}} [1 - e^{-2\tau_b}]$ as expected for a homogeneous slab of optical thickness $\tau_2 = \tau_b$ (see Eq. (A21)).

3.3 Estimation of the lidar attenuated backscatter

3.3.1 QlbiC estimate

To mimic the lidar problem, let’s assume that both layers consist of non-absorbing particles ($\varpi_1 = \varpi_2 = 1.0$) and that layer 1 scatters isotropically (with asymmetry factor $g_1 = 0$) and has a small optical thickness (say $\tau_1 = 0.05$), while layer 2 (the target layer) scatters according to a Henyey–Greenstein scattering phase function with asymmetry factor g_2 and optical thickness τ_2 . According to the **QlbiC** method, the contribution to the radiance reflectance from layer 2, the target layer, i.e., the single-scattering estimation of the radiance reflectance $R_{I,QlbiC}$ is given by the second term in Eq. (8):

$$\begin{aligned} R_{I,QlbiC} &= \frac{\varpi_2}{2S_2} [e^{-2\tau_1} - e^{-2\tau_2}] \\ &= \frac{\varpi_2}{2S_2} e^{-2\tau_1} [1 - e^{-2(\tau_2 - \tau_1)}] \quad [\text{sr}^{-1}]. \end{aligned} \tag{9}$$

The attenuated backscatter from the target layer (layer 2) is obtained by dividing by its vertical thickness Δz :

$$\begin{aligned} \beta_{QlbiC} &= \frac{1}{\Delta z} R_{I,QlbiC} \\ &= \frac{e^{-2\tau_1} \varpi_2}{\Delta z 2S_2} [1 - e^{-2(\tau_2 - \tau_1)}] \quad [\text{m}^{-1}\text{sr}^{-1}]. \end{aligned} \tag{10}$$

3.3.2 Lidar equation estimate

The attenuated backscatter coefficient (assuming a range bin of vertical extent Δz) from lidar measurements is given by the lidar equation:

$$\begin{aligned} \beta_{\text{lidar}} &= \frac{T^2}{\Delta z} \int_0^{\Delta z} \beta(z) e^{-2\alpha(z)z} dz \\ &= \frac{T^2}{\Delta z} \int_0^{\Delta z} \frac{\alpha(z)}{S(z)} e^{-2\alpha(z)z} dz \quad [\text{m}^{-1}\text{sr}^{-1}] \end{aligned} \tag{11}$$

where T^2 is the two-way transmittance, $\beta(z)$ [$\text{m}^{-1}\text{sr}^{-1}$] is the backscattering coefficient, $\alpha(z)$ [m^{-1}] is the extinction coefficient, $S(z)$ [sr] is the lidar ratio at altitude z , and Δz [m] is the bin size. If we assume that $\alpha(z)$ and $S(z)$ do not vary within the Δz vertical bin, then Eq. (11) yields

$$\beta_{\text{lidar}} = T^2 \frac{1}{\Delta z} \frac{1}{2S} [1 - e^{-2\alpha\Delta z}] \quad [\text{m}^{-1}\text{sr}^{-1}]. \tag{12}$$

Setting $T^2 = e^{-2\tau_1}$ and $\alpha\Delta z \approx \tau_2 - \tau_1$, we find that the attenuated backscatter results predicted by Eqs. (10) and (12) are the same, i.e., $\beta_{QlbiC} = \beta_{\text{lidar}}$ if $\varpi_2 = 1.0$ and $S = S_2$.

3.4 Generalization to an N -layer model

Assuming that all $N - 1$ layers above the target layer N have the same optical properties, then Eq. (10) should be replaced by

$$\beta_{QlbiC} = \frac{e^{-2\tau_{N-1}} \varpi_N}{\Delta z 2S_N} [1 - e^{-2(\tau_N - \tau_{N-1})}] \quad [\text{m}^{-1}\text{sr}^{-1}] \tag{13}$$

and Eq. (12) by

$$\beta_{\text{lidar}} = \frac{T_{N-1}^2}{\Delta z} \frac{1}{2S_N} [1 - e^{-2\alpha_N(\Delta z)_N}] \quad [\text{m}^{-1}\text{sr}^{-1}] \tag{14}$$

where $T_{N-1}^2 = e^{-2\tau_{N-1}}$ and $\alpha_N(\Delta z)_N = \tau_N - \tau_{N-1}$.

3.5 Numerical examples

The **QlbiC** method [12] allows one to quantify specific layer contributions of signals emerging from stratified, multilayered media based on solutions to the radiative transfer equation (RTE). As shown in the previous section, in the single-scattering approximation, the **QlbiC** solutions agree with those obtained using the standard lidar approach, but the **QlbiC** method also yields reliable results for optically thick, multiple-scattering aerosol and cloud layers. In the following, we use radiation reflected from (i) a multilayered atmosphere and (ii) a coupled atmosphere-ocean system to address the problem relevant for EM probing by a space-based lidar system. Hence, we will assume that the medium consists of either (i) *one single, multilayered slab* with a constant refractive index or (ii) *two adjacent multilayered slabs separated by a smooth interface* across which the real part of the refractive index m_r changes from one constant value $m_{r,1}$ in slab₁ to a different constant value $m_{r,2}$ in slab₂, such as for an atmosphere-water system.

To deal with the vertical variation of the scattering and absorption properties of the atmospheric constituents, it is necessary to treat it as a multilayered medium. Therefore, based on previous experience, we divided the atmosphere into 15 layers from top to bottom as illustrated in Fig. 1. This vertical stratification of the atmosphere in horizontal layers is sufficient to produce accurate radiances for a clear (cloud- and aerosol-free) atmosphere.

The key to accomplishing this quantification of the emerging radiance originating from any specific layer (or location) in the medium lies in our ability to compute and integrate the source function.¹ Thus, we are able to quantify the contribution to the emerging radiance from any particular layer of a stratified medium. Below we consider three different cases:

1. A clear atmosphere with *embedded aerosol layers*.
2. Same as item 1 above but contrasting continuous wave (CW) and *pulsed* lidar results.

¹ Knowing the source function is equivalent to knowing the complete solution of the radiative transfer problem.

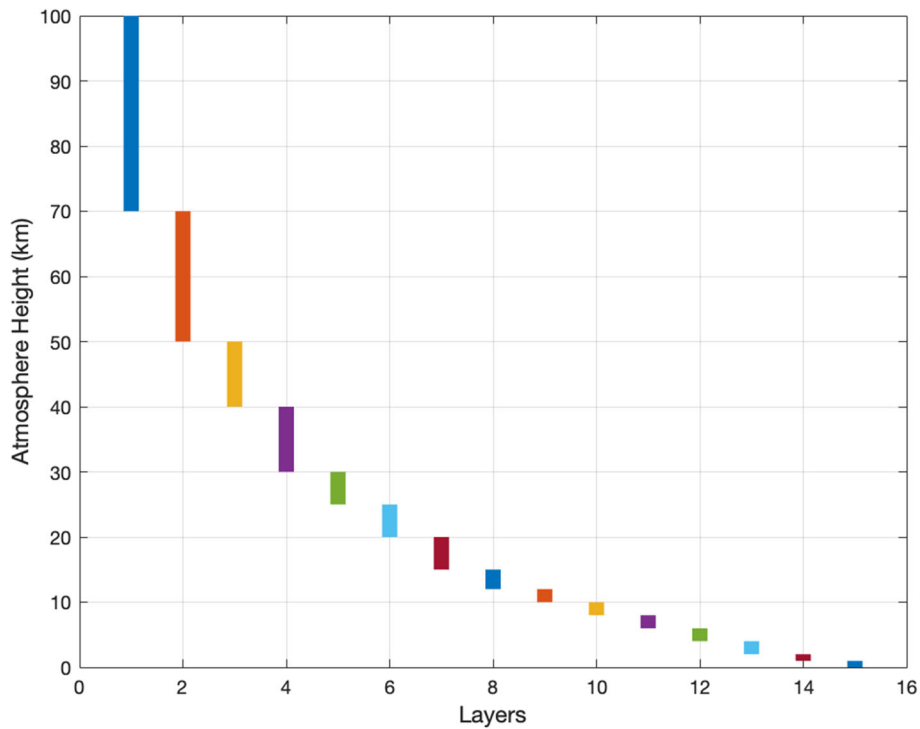


Fig. 1 Layering of the atmosphere

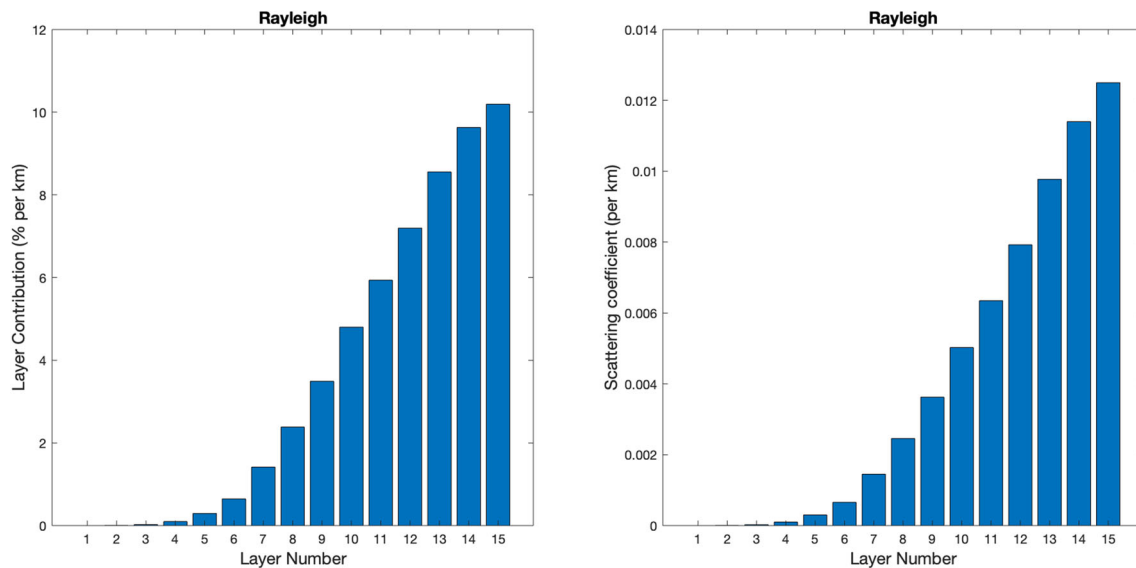


Fig. 2 Layer-by-layer (Ibl) contributions (per km) to the reflected radiance for a clear (US 76 Standard) atmosphere. Left panel: Percentage Ibl contributions. Right panel: Ibl contributions to the scattering coefficient. The total Rayleigh scattering optical depth at 532 nm was 0.134

3. An atmosphere overlying a body of water.

3.5.1 A clear atmosphere with *embedded aerosol layers*: CW lidar

First, we consider the CW lidar problem in which the steady-state RTE is solved, implying that the source function for any particular layer includes multiply-

scattered radiation from all layers below the layer of interest. Figure 2 shows the layer-by-layer (Ibl) contributions to the reflected radiance at the top of the atmosphere (TOA) for wavelength $\lambda = 532$ nm for this CW lidar configuration. As expected for an atmosphere that obeys the barometric law of near-exponential decrease with altitude in the bulk molecular number concentration, the major contributions to the reflected radiance

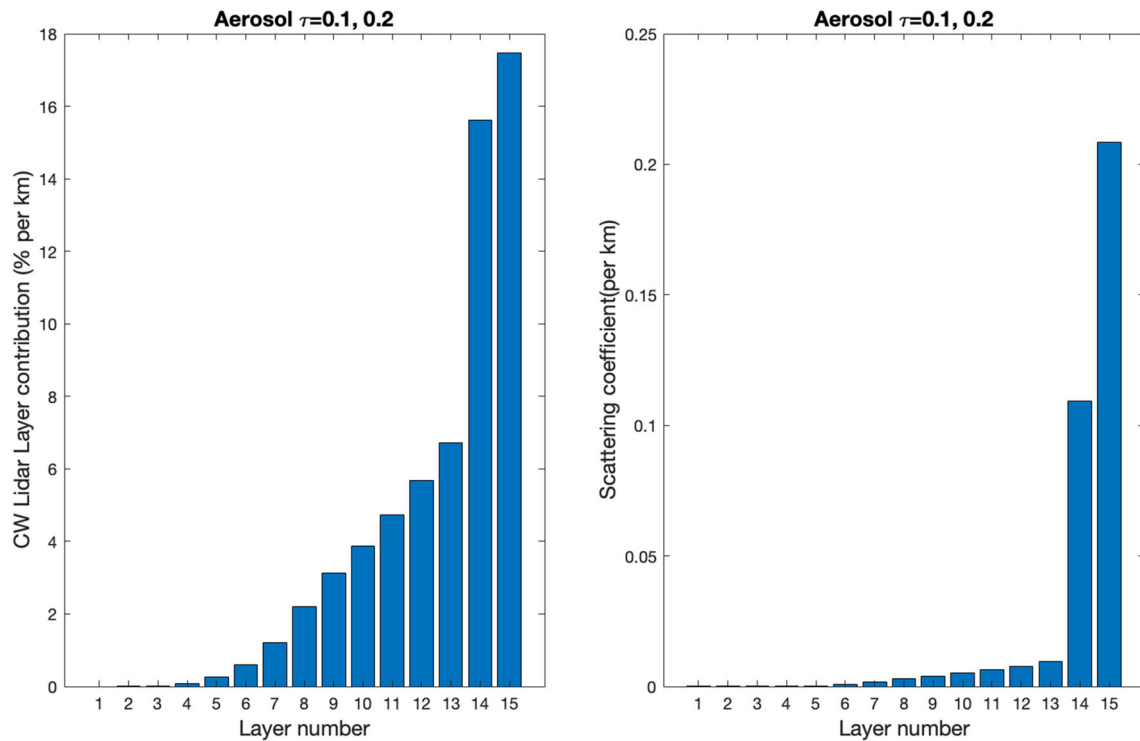


Fig. 3 Same as left part of Fig. 2 except that **aerosol particles** were mixed with the molecules in layers 14 and 15. The aerosol optical depth (AOD) was assumed to be 0.1 in layer 14 and 0.2 in layer 15, yielding a total AOD of **0.3**

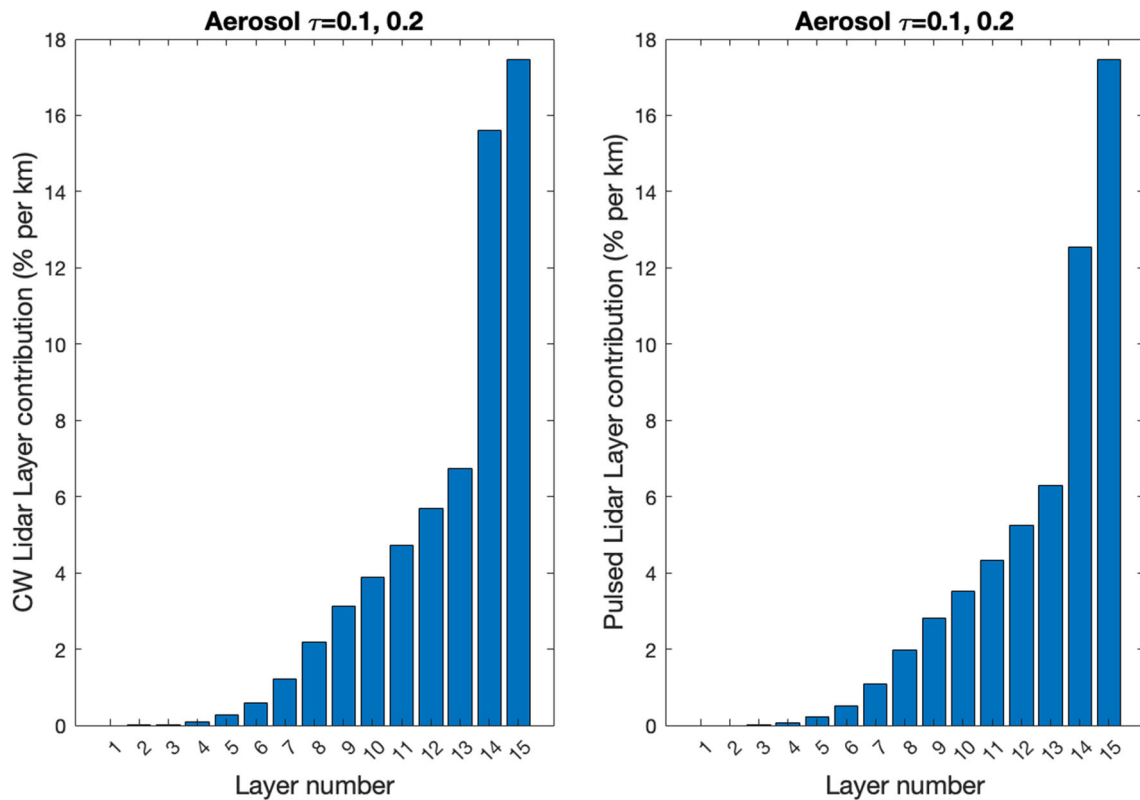


Fig. 4 Left panel: **CW** lidar (same as Fig. 3). Right panel: Same as left panel but for **pulsed** lidar. The aerosol optical depth (AOD) was assumed to be 0.1 in layer 14 and 0.2 in layer 15, yielding a total AOD of **0.3**

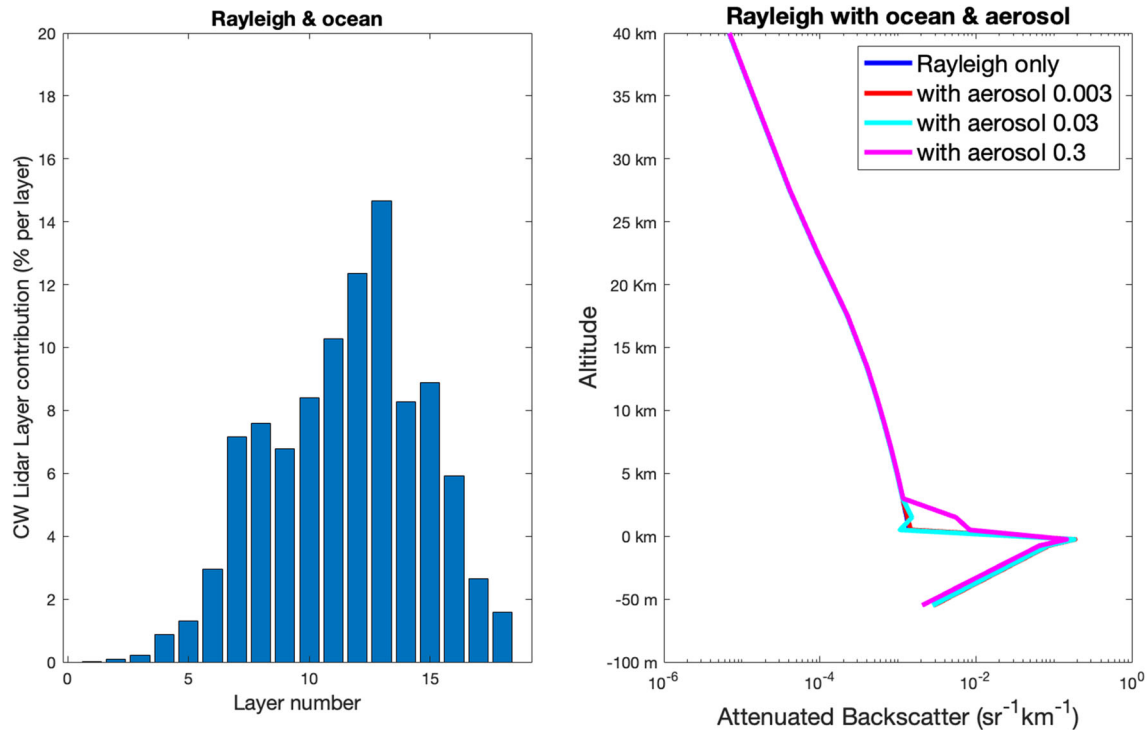


Fig. 5 Results pertaining to an atmosphere-ocean system assumed to consist of 15 atmospheric layers and three oceanic layers. Oceanic layers 16 and 17 each have a thickness of 5 m and contain pure water mixed with algae (pigmented particles), non-algal particulate matter, and Colored Dissolved Organic Matter (CDOM) impurities typical for coastal water. Layer 18 (10-100 m depth) is assumed to contain pure water. Left panel: Percentage **lbl** contributions (per layer). Right panel: Same as left panel but presented as reflectance profiles

at the TOA come from the layers close to the surface. To mimic the lidar problem, we assumed nadir incidence, i.e., a beam zenith angle of 0°, and a polar observation angle of 0°.

To demonstrate how aerosols impact the **lbl** contributions to the TOA radiance, we included an aerosol component in each of layers 14 and 15 (closest to the surface). This aerosol component was assumed to consist of weakly absorbing particles, homogeneously mixed with the molecules in layers 14 and 15. The **lbl** contributions to the TOA radiance for this case are shown in Fig. 3. Note that the largest **lbl** contribution to the TOA radiance comes from layer 15, and the next largest from layer 14 as expected since the aerosol optical thickness in layer 15 is twice that of layer 14.

3.5.2 Continuous wave (CW) versus Pulsed lidar

The results shown in Figs. 2 and 3 pertain to a CW lidar configuration. To address the pulsed lidar problem, we adopt the following approach:

- In the **CW** lidar problem: the source function for each layer contains contributions also from all layers, including those *below* a given layer of interest.
- To simulate the **pulsed** lidar problem, we must **omit** contributions from layers **below** the layer of interest. Hence, we may proceed as follows:

1. Starting at the top of the slab (atmosphere), we first solve a two-layer problem to get the **lbl** contribution from the second layer (counting from the top). The uppermost layer is optically very thin. Hence, we can ignore its possible contribution, and contributions from all layers below layer 2 are ignored.
2. Next, we solve the 3-layer problem to get the **lbl** contribution from layer 3, again ignoring contributions from all layers below layer 3.
3. Then, we continue in this manner until we have determined the **lbl** contributions from layer 4, layer 5, ..., layer *N* for a *N*-layer slab.

Results for the CW and pulsed lidar configurations are shown in Fig. 4. Note that the **pulsed** lidar configuration (right panel) yields smaller **lbl** contributions than the **CW** lidar configuration (left panel) as expected.

3.5.3 An atmosphere overlying a body of water

Our final example pertains to a clear atmosphere overlying a body of oceanic water. The atmosphere is assumed to consist of 15 layers, and the ocean is assumed to consist of three layers with a total thickness of 100 m. Each of the two uppermost ocean layers has a thickness of 5 m and contain pure water mixed

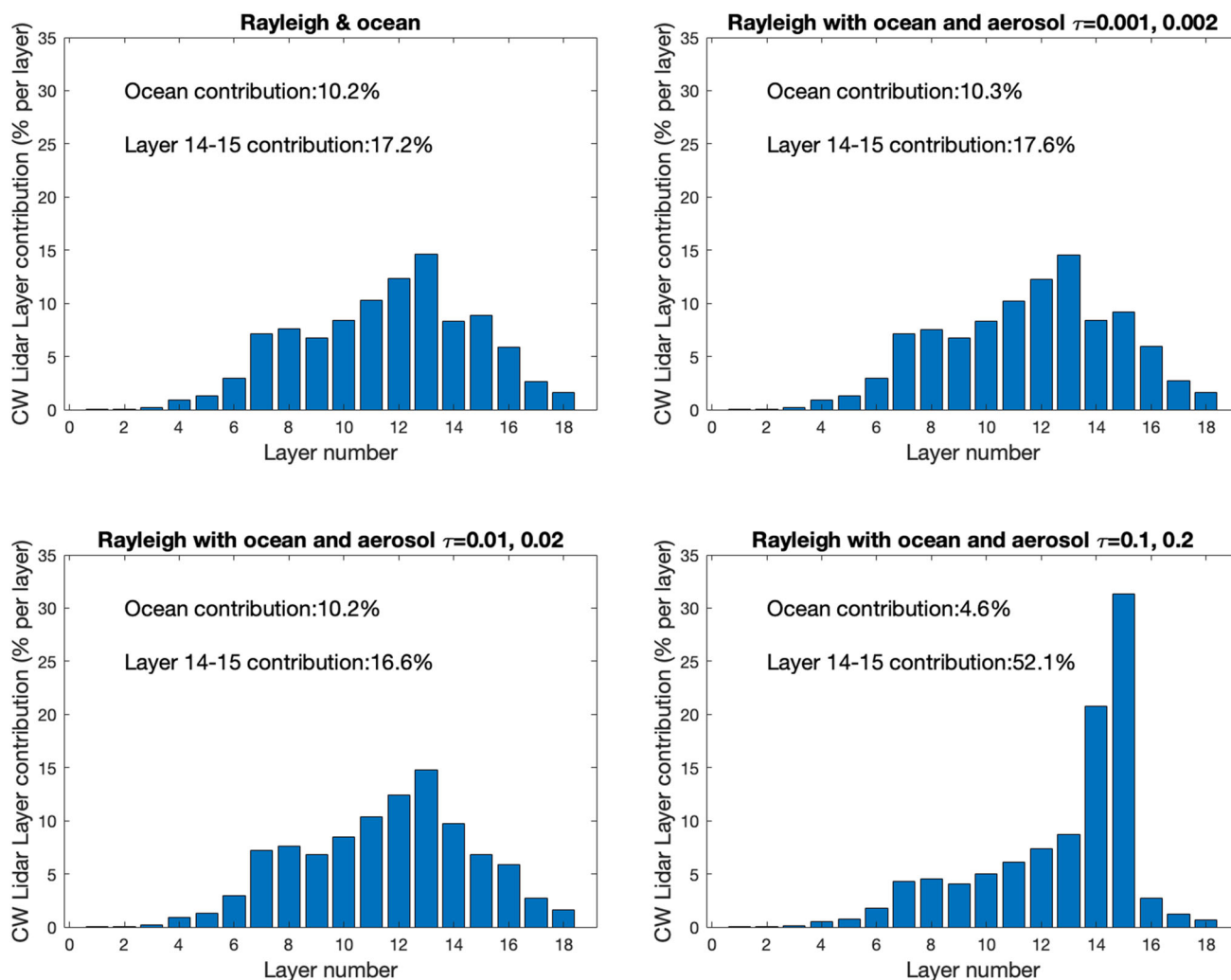


Fig. 6 Impact of adding aerosol particles in layers 14 and 15 at the bottom of the atmosphere. Percentage **lbl** contributions (per layer) for an atmosphere having Upper left: AOD = 0; Upper right: AOD = 0.003; Lower left: AOD = 0.03; Lower right: AOD = 0.3

with algae (chlorophyll concentration of $0.5 \text{ mg}\cdot\text{m}^{-3}$), a small amount of mineral particles ($0.005 \text{ g}\cdot\text{m}^{-3}$), and Colored Dissolved Organic Matter (CDOM) absorption coefficient, 0.01 m^{-1} at 443 nm.

Below 10 m depth, the water is assumed to be pure. The left panel of Fig. 5 shows **lbl** contributions. Note that the largest contribution from the ocean comes for the upper layer (layer 16). Layer 17 (below) is effectively shielded by the overlying layer 16, and very little light penetrates to layer 18. The right panel of Fig. 5 shows the same results as in the left panel, but presented as reflectance profiles as is common in the atmospheric lidar community. Please note that in Figs. 5 and 6 the percentage contributions are per layer (not per km as in Figs. 2, 3, 4).

Figure 6 shows the impact of adding aerosol particles in layers 14 and 15 at the bottom of the atmosphere. In the upper left panel of Fig. 6, no aerosol

particles were added, but in the upper right panel a small amount (AOD = 0.003) was added. We note that this small amount has almost negligible impact. The contribution from the water to the TOA radiance is about 10.3%, while that from the two aerosol layers is about 17.6%. As the AOD is increased to 0.03 (lower left panel), those contributions change to about 10.2% (ocean) and 16.6% (aerosols). Finally, the lower right panel shows that for a total AOD abundance of 0.3 in layers 14 and 15, these contributions change to 4.6% (ocean) and 52.1% (aerosols). These numbers are in general agreement with observations, and they illustrate that in order to retrieve reliable results for ocean properties from optical instruments deployed on space platforms, the impact of aerosols must be dealt with very carefully, since their abundance change in space and time.

4 Conclusion

We have shown that solutions to the RTE for a homogeneous slab of optical thickness τ_b yields a zenith radiance reflectance that for collimated beam incidence in the nadir direction can be expressed in terms of the lidar ratio \mathcal{S} simply as $R_{I,SSA} = \frac{1}{2\mathcal{S}}(1 - e^{-2\tau_b})$ in the single-scattering approximation. The lidar ratio, defined as the extinction coefficient divided by the 180° backscattering coefficient, is given by $\mathcal{S} = \mathcal{S}_{iso} = 4\pi$ for isotropic scattering, $\mathcal{S} = \mathcal{S}_{Ray} = \frac{8\pi}{3}$ for Rayleigh scattering, and $\mathcal{S} = \mathcal{S}_{HG} = \frac{4\pi(1+g)^2}{(1-g)}$ for Henyey–Greenstein (HG)scattering, where $g = \langle \cos \Theta \rangle$ is the scattering asymmetry factor and Θ is the scattering angle.

A simple two-layer model was used to show explicitly that in the single-scattering approximation an estimate of the attenuated backscatter coefficient based on the **QlbIC** method gives the same result as the lidar equation. As described in a recent paper [12], the **QlbIC** method applies to the continuous wave (CW) lidar problem. In Sect. 3.5.2, we extended the **QlbIC** method to be applicable to the pulsed lidar problem and showed that as expected the **pulsed** lidar configuration yields smaller **lbl** contributions than the **CW** lidar configuration.

In Sect. 3.5.3, an example was provided (Figs. 5 and 6) to illustrate the challenge encountered for ocean property retrievals from space observations due to the fact that a very significant fraction of the signal is due to aerosol scattering/absorption; typically only about 10% (or less) comes from the ocean. The contribution from molecules is easier to deal with because it depends largely on the total column amount of molecules which depends on pressure through the ideal gas law. Pressure measurements are commonly available.

Acknowledgements The authors wish to thank the NASA Remote Sensing Theory program and the NASA ESTO’s IIP program for supporting this research.

Author contributions

KS provided the theoretical concept and wrote the first draft of the paper. WL did the AccuRT/QlbIC computations under KS guidance. All co-authors contributed with critical feedback and ideas during the paper writing process.

Data Availability Statement This manuscript has no associated data or the data will not be deposited. [Authors’ comment: This article presents model calculations and makes use of no data that are not already available in papers cited in the article.]

Declarations

Conflict of interest Authors CW and JL were employed by Ball Aerospace Corp. The remaining authors declare that

the research was conducted in the absence of any commercial or financial relationships that could be construed as a potential conflict of interest. The raw data supporting the conclusions of this article will be made available by the authors, without undue reservation.

Open Access This article is licensed under a Creative Commons Attribution 4.0 International License, which permits use, sharing, adaptation, distribution and reproduction in any medium or format, as long as you give appropriate credit to the original author(s) and the source, provide a link to the Creative Commons licence, and indicate if changes were made. The images or other third party material in this article are included in the article’s Creative Commons licence, unless indicated otherwise in a credit line to the material. If material is not included in the article’s Creative Commons licence and your intended use is not permitted by statutory regulation or exceeds the permitted use, you will need to obtain permission directly from the copyright holder. To view a copy of this licence, visit <http://creativecommons.org/licenses/by/4.0/>.

Appendix A single-scattering solutions

A.1 Radiative Transfer Simulations of the radiance reflectance (R_I value)

Let’s assume that the angular scattering can be described by the synthetic Henyey–Greenstein scattering phase function expressed in terms of the asymmetry factor g by

$$p_{HG}(\cos \Theta) = \frac{1 - g^2}{(1 + g^2 - 2g \cos \Theta)^{3/2}}. \tag{A1}$$

To get the appropriate R_I value, for any scattering phase function (isotropic scattering ($g = 0$) or anisotropic scattering ($g \neq 0$)), we need to solve the pertinent radiative transfer equation (RTE), also when the single-scattering approximation is applicable. For simplicity, let’s consider a slab geometry. For the lidar problem, the R_I value is the upward radiance reflectance in the zenith direction (perpendicular to the slab). Since this R_I value is azimuth independent, we may use the azimuthally averaged RTE [13]

$$\pm \mu \frac{dI^\pm(\tau, \mu)}{d\tau} = I^\pm(\tau, \mu) - S^\pm(\tau, \mu), \tag{A2}$$

where $\mu \equiv \|\cos \theta\|$ ($0 \leq \mu \leq 1$). Letting $u = \cos \theta$, and taking u' as the dummy (integration) variable, the source function can be written [13]

$$S^\pm(\tau, \mu) = \frac{\varpi(\tau)}{2} \int_{-1}^1 du' p(\tau, u', \pm\mu) I(\tau, u') + X^\pm(\tau, -\mu_0, \mu) e^{-\tau/\mu_0} \tag{A3}$$

$$X^\pm(\tau, -\mu_0, \mu) = \varpi(\tau)F_0 \frac{p(\tau, -\mu_0, \pm\mu)}{4\pi} = \frac{\varpi(\tau)F_0}{\mathcal{S}} \tag{A4}$$

where $\mathcal{S} \equiv 4\pi/p(\tau, -\mu_0, \pm\mu)$, F_0 in the incident beam irradiance (normal to the direction of incidence) and $\theta_0 = \cos^{-1}\mu_0$ is the angle of incidence of the lidar beam. In Eq. (A2), $I^+(\tau, \mu)$ is the diffuse radiance in the upward direction with polar angles in the range $0 \leq \theta \leq \pi/2$, and $I^-(\tau, \mu)$ is the diffuse radiance in the downward direction with polar angles in the range $\pi/2 \leq \theta \leq \pi$. In Eq. (A4) $p(\tau, -\mu_0, \pm\mu)$ is the azimuthally averaged scattering phase function

$$p(\tau, -\mu_0, \pm\mu) = \frac{1}{2\pi} \int_0^{2\pi} d\phi p(-\mu_0, \phi'; \pm\mu, \phi). \tag{A5}$$

For a homogeneous slab with $\varpi(\tau) = \varpi$ and $p(\tau, u', \pm\mu) = p(u', \pm\mu)$, we assume (i) $\tau_0 = 0$ is the optical depth at the upper boundary (top of the slab); and (ii) τ_b is the optical depth at the lower boundary (bottom of the slab). Note that Eqs. (A2)–(A5) are valid for arbitrary values of τ in the range $\tau_0 \leq \tau \leq \tau_b$.

A.1.1 Single-scattering approximation (SSA)

In the single-scattering approximation, we ignore the integral (multiple-scattering) term in Eq. (A3) to obtain:

$$S^\pm(\tau, \mu) \approx X^\pm(-\mu_0, \mu)e^{-\tau/\mu_0} \tag{A6}$$

for a homogeneous slab. Integration of Eq. (A2) yields the following single-scattering approximation (SSA) to the upward radiance [13]:

$$I_{SSA}^+(\tau, -\mu_0, \mu) = \frac{\mu_0 X^+(-\mu_0, \mu)}{(\mu_0 + \mu)} \left[e^{-\tau/\mu_0} - e^{-[(\tau_b - \tau)/\mu + \tau_b/\mu_0]} \right]. \tag{A7}$$

Case 1: Isotropic scattering

For a homogeneous slab with isotropic scattering, we have $p_{iso}(-\mu_0, \pm\mu) = 1$, and hence (Eq. (A4) yields $X^+(-\mu_0, \mu) = \varpi F_0/4\pi$. Then Eq. (A7) simplifies to

$$I_{SSA}^+(\tau, -\mu_0, \mu) = \frac{\mu_0 \varpi F_0}{4\pi(\mu_0 + \mu)} \left[e^{-\tau/\mu_0} - e^{-[(\tau_b - \tau)/\mu + \tau_b/\mu_0]} \right]. \tag{A8}$$

Hence, the upward radiance in the zenith direction ($\mu = 1$) becomes

$$I_{SSA}^+(\tau, -\mu_0, 1) = \frac{\mu_0 \varpi F_0}{4\pi(\mu_0 + 1)} \left[e^{-\tau/\mu_0} - e^{-[(\tau_b - \tau) + \tau_b/\mu_0]} \right] \tag{A9}$$

which for normal incidence ($\mu_0 = 1$) and $F_0 = 1.0$ yields:

$$I_{SSA}^+(\tau, -1, 1) = \frac{\varpi}{8\pi} \left[e^{-\tau} - e^{-(2\tau_b - \tau)} \right] = \frac{\varpi}{2\mathcal{S}_{iso}} \left[e^{-\tau} - e^{-(2\tau_b - \tau)} \right]. \tag{A10}$$

where the lidar ratio, defined as the extinction to backscatter ratio

$$\mathcal{S}_{iso} = 4\pi \text{ [sr]}$$

for isotropic scattering. Hence, for conservative scattering ($\varpi = 1.0$) the radiance reflectance becomes

$$R_{I,iso} = I_{SSA}^+(0, -1, 1) = \frac{1}{2\mathcal{S}_{iso}} \left[1 - e^{-2\tau_b} \right] \text{ [sr}^{-1}\text{]}. \tag{A11}$$

Case 2: Rayleigh scattering For a homogeneous slab with Rayleigh scattering, we have $p_{Ray}(-\mu_0, \pm\mu) = \frac{3}{4}(1 + \cos^2 \Theta)$, and hence $X^+(-\mu_0, \mu) = \frac{\varpi F_0}{4\pi} \frac{3}{4}(1 + \cos^2 \Theta)$ according to Eq. (A4), and Eq. (A7) becomes

$$I_{SSA}^+(\tau, -\mu_0, \mu) = \frac{\mu_0 \varpi F_0}{(\mu_0 + \mu)} \frac{p_{Ray}(-\mu_0, \mu, g)}{4\pi} \left[e^{-\tau/\mu_0} - e^{-[(\tau_b - \tau)/\mu + \tau_b/\mu_0]} \right]. \tag{A12}$$

Since the scattering angle Θ is related to the polar angles (θ' and θ) and azimuth angles (ϕ' and ϕ) by

$$\cos \Theta = uu' + \sqrt{1 - u^2} \sqrt{1 - u'^2} \cos(\phi' - \phi) \tag{A13}$$

we have ($u' = \cos \theta'$ and $u = \cos \theta$)

$$p_{Ray}(u', \phi'; u, \phi) = \frac{3}{4} \left(1 + [uu' + \sqrt{1 - u^2} \sqrt{1 - u'^2} \cos(\phi' - \phi)]^2 \right) = \frac{3}{4} (a_1 + a_2 \cos(\phi' - \phi) + a_3 \cos^2(\phi' - \phi)) \tag{A14}$$

where

$$a_1 = (1 + (uu')^2), \quad a_2 = 2uu' \sqrt{1 - u^2} \sqrt{1 - u'^2}, \quad \text{and } a_3 = (1 - u^2)(1 - u'^2). \tag{A15}$$

Hence, the azimuthally averaged phase function

$$p_{Ray}(u', u) = \frac{1}{2\pi} \int_0^{2\pi} d\phi p_{Ray}(u', \phi'; u, \phi) = \frac{1}{2\pi} \frac{3}{4} \int_0^{2\pi} d\phi (a_1 + a_2 \cos(\phi' - \phi) + a_3 \cos^2(\phi' - \phi)) \tag{A16}$$

becomes (setting $u' = -\mu_0 = -1$ and $u = 1$, implying $a_1 = 2, a_2 = a_3 = 0$, see Eq. (A15)):

$$p_{\text{Ray}}(-1, 1) = \frac{3}{2} \Rightarrow \frac{1}{\mathcal{S}} = \frac{p_{\text{Ray}}(-1, 1)}{4\pi} = \frac{3}{8\pi}. \quad (\text{A17})$$

Hence,

$$\mathcal{S}_{\text{Ray}} = \frac{8\pi}{3} \text{ [sr]} \Rightarrow \frac{1}{2\mathcal{S}_{\text{Ray}}} = \frac{3}{16\pi} \text{ [sr}^{-1}\text{]}$$

and (see Eq. (A12))

$$R_{I,\text{Ray}} = I_{\text{SSA}}^+(0, -1, 1) = \frac{1}{2\mathcal{S}_{\text{Ray}}}(1 - e^{-2\tau_b}) \text{ [sr}^{-1}\text{]}. \quad (\text{A18})$$

Case 3: Henyey–Greenstein (HG) scattering
 HG scattering is defined by the one-parameter scattering phase function ($u = \cos \theta, u' = \cos \theta'$) given by Eq. (A1), $p_{\text{HG}}(\cos \Theta) = p_{\text{HG}}(u', \phi'; u, \phi)$, where the scattering angle Θ is related to the polar and azimuth angles by Eq (A13). The azimuthally averaged scattering phase function is:

$$p_{\text{HG}}(u', u, g) = \frac{1}{2\pi} \int_0^{2\pi} d\phi p_{\text{HG}}(u', \phi'; u, \phi). \quad (\text{A19})$$

Thus, according to Eq. (A4)

$$X^+(-\mu_0, \mu) = \varpi F_0 \frac{p_{\text{HG}}(-\mu_0, \mu, g)}{4\pi}$$

and Eq. (A7) becomes

$$I_{\text{SSA}}^+(\tau, -\mu_0, \mu) = \frac{\mu_0 \varpi F_0}{(\mu_0 + \mu)} \frac{p_{\text{HG}}(-\mu_0, \mu, g)}{4\pi} \left[e^{-\tau/\mu_0} - e^{-[(\tau_b - \tau)/\mu + \tau_b/\mu_0]} \right]. \quad (\text{A20})$$

Hence, for perpendicular incidence ($\mu_0 = 1.0$) with $F_0 = 1.0$, for conservative scattering ($\varpi = 1.0$) the radiance reflectance in the zenith direction ($\mu = 1.0$) becomes

$$R_{I,\text{HG}} = I_{\text{SSA}}^+(0, -1, 1) = \frac{1}{8\pi} p_{\text{HG}}(-1, 1, g) [1 - e^{-2\tau_b}] = \frac{1}{8\pi} \frac{(1-g)}{(1+g)^2} [1 - e^{-2\tau_b}]. \quad (\text{A21})$$

or

$$R_{I,\text{HG}} = \frac{1}{2\mathcal{S}_{\text{HG}}} [1 - e^{-2\tau_b}] \text{ [sr}^{-1}\text{]} \quad \mathcal{S}_{\text{HG}} = \frac{4\pi(1+g)^2}{(1-g)} \text{ [sr]}. \quad (\text{A22})$$

Equation (A21) follows because $p_{\text{HG}}(u', \phi'; u, \phi) = (1 - g^2)/[(1 + g^2 - 2g \cos \Theta)^{3/2}]$. Hence,

$$p_{\text{HG}}(u', \phi'; u, \phi) = \frac{1-g^2}{(1+g^2-2g[uu'+\sqrt{1-u^2}\sqrt{1-u'^2}\cos(\phi'-\phi)])^{3/2}} \quad (\text{A23})$$

and direct integration yields:

$$p_{\text{HG}}(u', u, g) = \frac{1}{2\pi} \int_0^{2\pi} d\phi p_{\text{HG}}(u', \phi'; u, \phi) = \frac{1}{2\pi} \int_0^{2\pi} \frac{a_1 d\phi}{(a_2 - a_3 \cos(\phi' - \phi))^{3/2}} \quad (\text{A24})$$

where $a_1 = (1 - g^2)$, $a_2 = 1 + g^2 - 2gu'u$, and $a_3 = 2g\sqrt{1 - u^2}\sqrt{1 - u'^2}$. For the special case $u' = -1, u = 1$, the cosine term in the denominator of Eq. (A24) vanishes ($a_3 = 0$), and we get

$$p_{\text{HG}}(-1, 1, g) = p_{\text{HG}}(u' = -1, u = 1, g) = \frac{(1 - g^2)}{(1 + g^2 + 2g)^{3/2}} = \frac{(1 - g)}{(1 + g)^2}.$$

A.1.2 Summary

These examples demonstrate that in the single-scattering approximation the radiance reflectance can be expressed in terms of the lidar ratio as:

$$R_{I,\text{SSA}} = \frac{1}{2\mathcal{S}}(1 - e^{-2\tau_b}) \quad (\text{A25})$$

where $\mathcal{S} = \mathcal{S}_{\text{iso}} = 4\pi$ for an isotropic scattering phase function;

$\mathcal{S} = \mathcal{S}_{\text{Ray}} = \frac{8\pi}{3}$ for a Rayleigh scattering phase function;

$\mathcal{S} = \mathcal{S}_{\text{HG}} = \frac{4\pi(1+g)^2}{(1-g)}$ for a HG scattering phase function.

References

1. S. Burton, M. Vaughan, R. Ferrare, C. Hostetler, Separating mixtures of aerosol types in airborne high spectral resolution lidar data. *Atmos. Measure. Tech.* **7**, 419 (2014)
2. J. Hair, C. Hostetler, Y. Hu, M. Behrenfeld, C. Butler, D. Harper, R. Hare, T. Berko, A. Cook, J. Collins et al., Combined atmospheric and ocean profiling from an airborne high spectral resolution lidar, In *EPJ Web of Conferences* (p. 22001). *EDP Sciences* **119**, (2016)
3. T.J. Thorsen, Q. Fu, J.M. Comstock, C. Sivaraman, M.A. Vaughan, D.M. Winker, D.D. Turner, Macrophysical properties of tropical cirrus clouds from the calipso

- satellite and from ground-based micropulse and raman lidars. *J. Geophys. Res. Atmos.* **118**, 9209–9220 (2013)
4. M.J. Behrenfeld, Y. Hu, C.A. Hostetler, G. Dall’Olmo, S.D. Rodier, J.W. Hair, C.R. Trepte, Space-based lidar measurements of global ocean carbon stocks. *Geophys. Res. Lett.* **40**, 4355–4360 (2013)
 5. M.J. Behrenfeld, Y. Hu, R.T. Omalley, E.S. Boss, C.A. Hostetler, D. Siegel, J.L. Sarmiento, J. Schulien, J.W. Hair, X. Lu et al., Annual boom-bust cycles of polar phytoplankton biomass revealed by space-based lidar. *Nat. Geosci.* **10**(118), 2017 (2017)
 6. C.A. Hostetler, M.J. Behrenfeld, Y. Hu, J.W. Hair, J.A. Schulien, Spaceborne lidar in the study of marine systems. *Annu. Rev. Marine Sci.* **10**, 121–147 (2018)
 7. R.J. Hogan, Fast approximate calculation of multiply scattered lidar returns. *Appl. Opt.* **45**, 5984–5992 (2006)
 8. C. Weitkamp, Lidar: range-resolved optical remote sensing of the atmosphere. Springer Science & Business **102**, (2006)
 9. R.J. Hogan, Fast lidar and radar multiple-scattering models. part i. Small-angle scattering using the photon variance-covariance method. *J. Atmos. Sci.* **65**, 3621–3635 (2008)
 10. R.J. Hogan, A. Battaglia, Fast lidar and radar multiple-scattering models. part ii. Wide-angle scattering using the time-dependent two-stream approximation. *J. Atmos. Sci.* **65**, 3636–3651 (2008)
 11. K. Mitra, J.H. Churnside, Transient radiative transfer equation applied to oceanographic lidar. *Appl. Opt.* **38**, 889–895 (1999)
 12. Knut Stamnes, Wei Li, Snorre Stamnes, Hu. Yongxiang, Yingzhen Zhou, Nan Chen, Yongzhen Fan, Børge Hamre, Lu. Xiaomei, Yuping Huang, Carl Weimer, Jennifer Lee, Xubin Zeng, Jakob Stamnes, A novel approach to solve forward/inverse problems in remote sensing applications. *Front. Remote Sens.* **3**, 10225447 (2022)
 13. K. Stamnes, G. E. Thomas, J. J. Stamnes, Radiative Transfer in the Atmosphere and Ocean, Cambridge University Press, second edition, (2017)